SUPPLEMENTARY DATA

ANALYTICAL METHODS

Electron Probe Microanalysis (EPMA)

A Cameca SXFive electron microprobe at Syracuse University was used for analysis of trace Zr in rutile, quantification of major and minor elements in silicate mineral phases, and quantitative mapping of major and minor element distributions. All measurements were performed using a 15 kV accelerating voltage.

Five wavelength dispersive spectrometers were used for trace element analysis by EPMA. Elements were standardized using silicate and oxide mineral standards by adjusting the beam current to attain ~12,000 counts per second on gas-flow proportional counters. Analysis of Zr in rutile was performed using a 200 nA beam current and a focused beam. Zirconium Kα X-rays were diffracted with large PET diffraction crystals (22 x 60 mm) and simultaneously counted on four spectrometers (400 seconds peak, 200 seconds background). The uncertainty on individual measurements is 20 ppmw and individual measurements have a 5 ppmw detection limit (Osborne et al., 2019). Rutile reference materials with 400 ppm Zr were measured throughout the duration of the analytical session to ensure accuracy of results.

Major element oxide compositional maps (Al, Si, Mg, Ti, Cr, Mn, Ca, Na, K, Fe) were collected using a 200 nA beam current, 0.005 second dwell time, and 5 μm stage-step size over a 10.24 mm^2 area. Quantitative spot analyses of all major mineral phases present (garnet, phengite, paragonite, epidote, quartz, albite, chlorite, chloritoid) were collected using a 20 nA beam current. Anhydrous minerals were analyzed with a focused beam, whereas hydrous minerals were analyzed using a 5 μm beam diameter. All quantitative spot analyses (n = 372) were collected from minerals within the mapped area.

Quantitative EPMA X-Ray Map Data Reduction

Quantitative maps were derived using MATLAB®-based XMapTools software (Lanari et al., 2014). Quantitative spot analyses were used as internal standards to quantify the composition of all pixels within the collected EPMA WDS X-ray maps. Individual mineral phases were isolated from the X-ray maps by plotting all pixels on binary and ternary plots and selecting clusters of pixels. Masks were created from each cluster of pixels that represented a given mineral. A border removing correction was applied to major mineral phases (i.e. garnet, quartz, phengite, and paragonite) to eliminate mixing pixels between mineral phases. Each mineral was standardized using quantitative spot analyses as internal references in the mapped area. Structural formulae of each mineral were derived using the automated routines for garnet, white micas, epidote, chlorite, and feldspar in XMapTools (Lanari et al., 2014).

Raman Spectroscopy

A Renishaw inVia Raman microprobe at Syracuse University was used for all Raman measurements. A 532 nm laser was focused onto specimens with a 100X microscope objective (N.A.=0.9) and Raman shifted light was statically dispersed with 1800 groove/mm gratings onto charged-couple devices resulting in spectral resolution of 0.5 cm^{-1}. The spectrometer was calibrated against neon lines and a silicon standard. Spectral accuracy and linearity were checked throughout each analytical session by measuring the 520.5 cm^{-1} Raman band of a silicon standard, and the Raman bands of a synthetic quartz reference material from the Westinghouse Corporation. All Raman spectra were acquired for 20 seconds and measured at room conditions of 23°C and 1 bar. Spectra were not processed or corrected prior to peak fitting using Renishaw software. Errors on fitted band positions are ~0.2 to 0.3 cm^{-1}.

A Raman depth profile was performed to determine the thickness (Z-dimension) of the relict coesite. The Raman microscope was equipped with a Renishaw MS20 high-speed encoded stage with an encoder resolution of 100 nm step size to track stage *X*-*Y*-*Z* position. The target was first brought into optimal ocular focus. The thickness was estimated by optical focusing on the top and bottom of the target. *X*-*Y*-*Z* coordinates were recorded using the optically encoded Renishaw automated stage at the 100x setting (0.1 μm step). This enabled us to ensure that the resolution of depth transects was sufficient to determine target thickness with an appropriate step size. The depth profile commenced 5 μm beneath the depth at which the relict coesite was in optimum optical focus (25 μm beneath the surface of the thin section) and progressed 10 μm towards the surface of the thin section at 0.2 μm increments. Raman spectra were processed for band positions and intensities of diagnostic 464 cm^{-1} (quartz), 521 cm^{-1} (coesite), and 910 cm^{-1} (garnet) bands (Figure 3d).

To characterize the *X*-*Y* dimensions of the relict coesite, two-dimensional (*X*-*Y*) Raman mapping was conducted using a 0.2 μm step size over a 20.25 μm^2 area at the depth corresponding to the highest intensity for the 521 cm^{-1} band. Raman data were processed for the intensity of the 521 cm^{-1} band of coesite using the Renishaw software. Map results were exported and plotted using MATLAB®.

THERMOBAROMETRIC METHODS

Quartz-in-Garnet Elastic Barometry

Elastic thermobarometry uses the Raman band positions of an elastically isolated inclusion (i.e. not fractured, near other inclusions or along grain boundaries) in a host mineral in conjunction with the Grünesien tensor to calculate the remnant strain and, therefore, remnant inclusion pressures (Murri et al., 2018; Angel et al., 2019; Bonazzi et al., 2019). The Equations of State for

the host and inclusion minerals can be used with the remnant inclusion pressures in an elastic model to calculate curves of relative volume equivalency in *P–T* space (isomekes) that represent the possible conditions of inclusion entrapment (Angel et al., 2017b).

Remnant inclusion pressures (P_{inc}) were calculated from room temperature measurements of the 128, 206, and 464 cm^{-1} Raman bands of quartz inclusions in garnet using an elastic-tensor calculation (Murri et al., 2018; Bonazzi et al., 2019) ($P_{inc}^{e.t.}$). The elastic-tensor was chosen for calculating P_{inc} because it inherently accounts for quartz elastic anisotropy at room *P–T* conditions (Bonazzi et al., 2019). The stRAinMAN software (Angel et al., 2019) was used to calculate strains $\varepsilon_1+\varepsilon_2$ and ε_3 imposed on the quartz crystallographic axes. Strains were used in conjunction with elastic constants of quartz at room *P–T* conditions to calculate $P_{inc}^{e.t.}$ (Wang et al., 2015). A matrix of the elastic tensor was derived using the elastic constants of Wang et al., (2015) and symmetry constraints of trigonal α-quartz (Nye, 1957). A stress matrix was calculated using matrix multiplication of the elastic tensor matrix and the strain matrix. To determine $P_{inc}^{e.t.}$, the components of the stress matrix were summed and divided by three.

Isomekes define the *P–T* points along which inclusions with a specific P_{inc} could have been entrapped and were calculated using Eq. 6 of Angel et al.(2017). Quartz volumes were calculated using a *P–T–V* equation of state and parameters for the full Landau transition and curved α-β phase boundary model (Angel et al., 2017a). The Tait equation of state described in Holland and Powell, (2011) and Equation of State parameters listed in Gonzalez et al., (2019) were used to calculate garnet volumes. In order to estimate *P–T* of inclusion entrapment, isomekes were combined with a complimentary thermometric determination (Thomas and Spear, 2018).

Zr-in-Rutile Trace Element Thermobarometry

A re-calibration (Kohn, 2020) of Tomkins et al.'s, (2007) and Hofmann et al., (2013) pressure-temperature dependent solubility model was used to determine temperatures based on Zr concentrations in rutile. The re-calibrated Zr-in-rutile solubility model reduces the propagated uncertainty on temperature determinations to ±15 °C. To constrain *P–T* conditions, the α-quartz solubility model of Kohn (2020) was used to constrain *P–T* conditions for the garnet porphyroblast core-mantle regions (Fig. S3, S4), whereas the coesite solubility model of Kohn (2020) was used to constrain *P–T* conditions for the garnet rim (Fig. S5).

Supplementary Data References

Angel, R.J., Alvaro, M., Miletich, R., and Nestola, F., 2017a, A simple and generalised P–T–V EoS for continuous phase transitions, implemented in EosFit and applied to quartz: Contributions to Mineralogy and Petrology, v. 172, p. 1–15, doi:10.1007/s00410-017-1349-x.

Angel, R.J., Mazzucchelli, M.L., Alvaro, M., and Nestola, F., 2017b, EosFit-Pinc: A simple GUI for host-inclusion elastic thermobarometry: American Mineralogist, v. 102, p. 1957–1960, doi:10.2138/am-2017-6190.

Angel, R.J., Murri, M., Mihailova, B., and Alvaro, M., 2019, Stress, strain and Raman shifts: Zeitschrift fur Kristallographie - Crystalline Materials, v. 234, p. 129–140, doi:10.1515/zkri-2018-2112.

Bonazzi, M., Tumiati, S., Thomas, J.B., Angel, R.J., and Alvaro, M., 2019, Assessing the reliability of elastic geobarometry methods: Lithos,.

Gonzalez, J.P., Thomas, J.B., Baldwin, S.L., and Alvaro, M., 2019, Quartz-in-garnet and Ti-in-quartz thermobarometry: Methodology and first application to a quartzofeldspathic gneiss from eastern Papua New Guinea: Journal of Metamorphic Geology, v. 37, p. 1193–1208,

doi:10.1111/jmg.12508.

Hofmann, A.E., Baker, M.B., and Eiler, J.M., 2013, An experimental study of Ti and Zr partitioning among zircon, rutile, and granitic melt: Contributions to Mineralogy and Petrology, v. 166, p. 235–253, doi:10.1007/s00410-013-0873-6.

Holland, T.J.B., and Powell, R., 2011, An improved and extended internally consistent thermodynamic dataset for phases of petrological interest, involving a new equation of state for solids: Journal of Metamorphic Geology, v. 29, p. 333–383, doi:10.1111/j.1525-1314.2010.00923.x.

Kohn, M.J., 2020, A refined zirconium-in-rutile thermometer: American Mineralogist, p. 1–25, doi:10.2138/am-2020-7091.

Lanari, P., Vidal, O., De Andrade, V., Dubacq, B., Lewin, E., Grosch, E.G., and Schwartz, S., 2014, XMapTools: A MATLAB©-based program for electron microprobe X-ray image processing and geothermobarometry: Computers and Geosciences, v. 62, p. 227–240, doi:10.1016/j.cageo.2013.08.010.

Murri, M., Mazzucchelli, M.L., Campomenosi, N., Korsakov, A. V., Prencipe, M., Mihailova, B.D., Scambelluri, M., Angel, R.J., and Alvaro, M., 2018, Raman elastic geobarometry for anisotropic mineral inclusions: American Mineralogist, v. 103, p. 1869–1872, doi:10.2138/am-2018-6625CCBY.

Nye, J.F., 1957, Physical Properties of Crystals: Oxford, Oxford University Press, 329 p.

Osborne, Z.R., Thomas, J.B., Nachlas, W.O., Baldwin, S.L., Holycross, M.E., Spear, F.S., and Watson, E.B., 2019, An experimentally calibrated thermobarometric solubility model for titanium in coesite (TitaniC): Contributions to Mineralogy and Petrology, v. 5, p. 1–13, doi:10.1007/s00410-019-1575-5.

Thomas, J.B., and Spear, F.S., 2018, Experimental study of quartz inclusions in garnet at pressures up to 3.0 GPa: evaluating validity of the quartz-in-garnet inclusion elastic thermobarometer: Contributions to Mineralogy and Petrology, v. 173, p. 1–14, doi:10.1007/s00410-018-1469-y.

Tomkins, H.S., Powell, R., and Ellis, D.J., 2007, The pressure dependence of the zirconium-in-rutile thermometer: Journal of Metamorphic Geology, v. 25, p. 703–713, doi:10.1111/j.1525-1314.2007.00724.x.

Wang, J., Mao, Z., Jiang, F., and Duffy, T.S., 2015, Elasticity of single-crystal quartz to 10 GPa: Physics and Chemistry of Minerals, v. 42, p. 203–212, doi:10.1007/s00269-014-0711-z.

Supplementary Data Table Captions:

Table S1: EPMA WDS spot analyses used as internal standards to make the quantitative WDS X-ray maps. Tables denoted as “header” contain the analytical conditions and standards.

Table 2: Raw Raman spectra from Figure 3c as .txt files.

Table 3: QuiG elastic thermobarometry data.

Table 4: Zr concentrations in ppm by weight.

Supplementary Data Figure Captions:

Figure S1: Photomicrographs of the Tillotson Peak Complex garnet metapelite. A. Fractured garnet containing abundant inclusions. Chl: chlorite, Cld: chloritoid, Ep: epidote, Grt: garnet, Qz: quartz, Rt: rutile. B. PPL photomicrograph of the metamorphic fabric. C. Crossed polarized light photomicrograph of the metamorphic fabric.

Figure S2: Plot of Zr concentration averages from matrix and inclusion rutile. Rutile inclusions are separated by location within the garnet.

Figure S3: Intersection of the QuiG isomekes with the Zr-in-rutile measurements from the garnet core. Zr-in-rutile isopleths calculated using the Tomkins et al., (2007) solubility model are plotted for comparison.

Figure S4: Intersection of the QuiG isomekes with the Zr-in-rutile measurements from the garnet mantle. Zr-in-rutile isopleths calculated using the Tomkins et al., (2007) solubility model are plotted for comparison.

Figure S5: Intersection of the QuiG isomekes with the Zr-in-rutile measurements from the garnet rim. Zr-in-rutile isopleths calculated using the Tomkins et al., (2007) solubility model, and Kohn (2020) calibrations for both quartz and coesite are plotted for comparison.

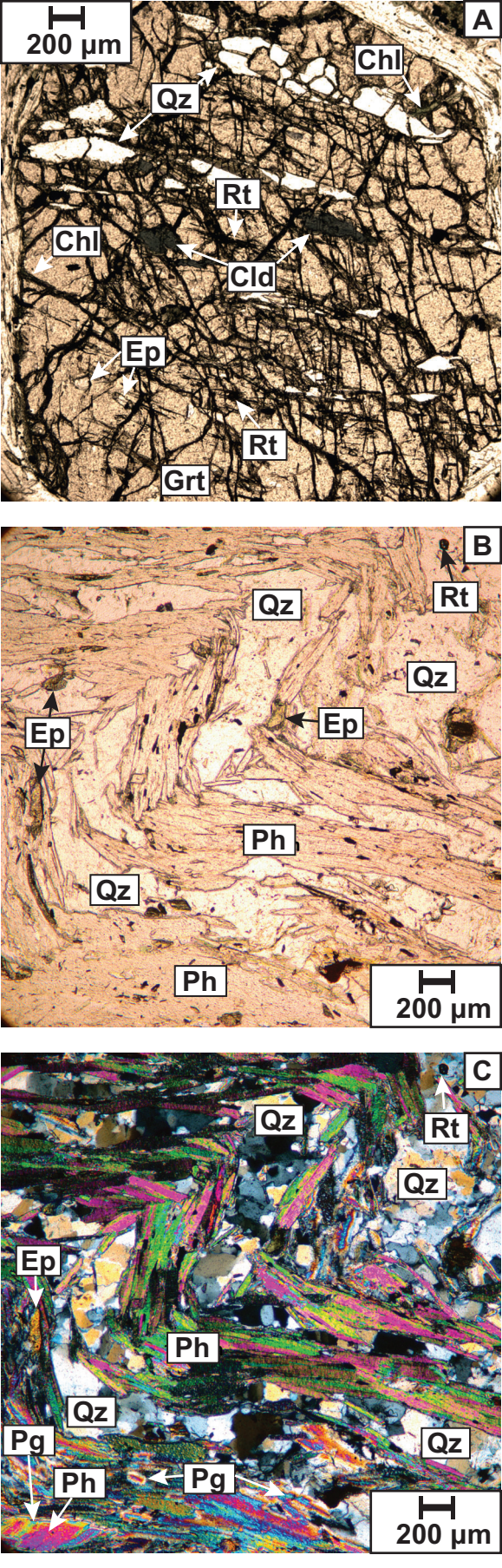

Supplementary Figure 1

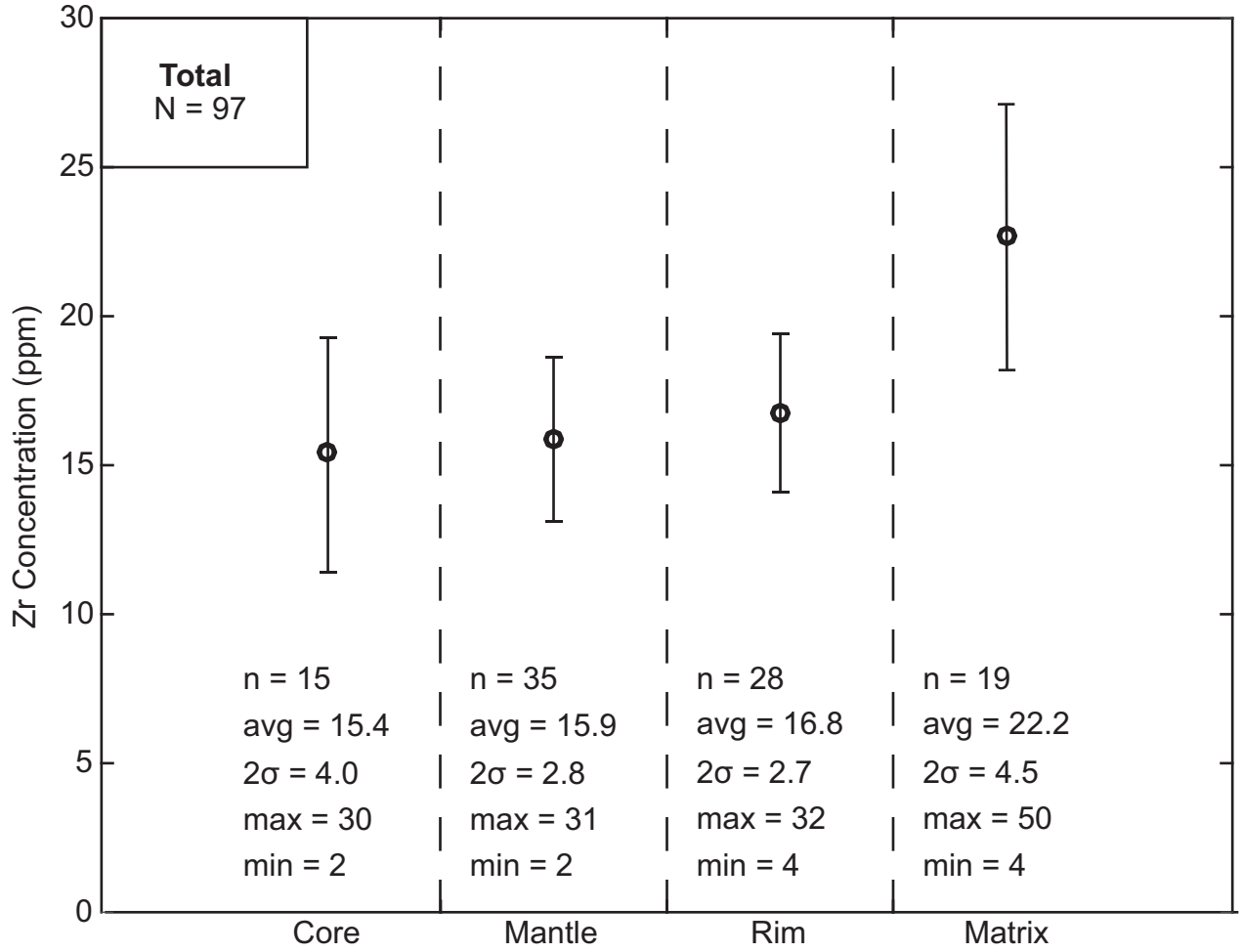
Total
N = 97
Zr Concentration (ppm)
30
25
20
15
10
5
0
n = 15
avg = 15.4
2σ = 4.0
max = 30
min = 2
n = 35
avg = 15.9
2σ = 2.8
max = 31
min = 2
n = 28
avg = 16.8
2σ = 2.7
max = 32
min = 4
n = 19
avg = 22.2
2σ = 4.5
max = 50
min = 4
Core
Mantle
Rim
Matrix

Fig. S2

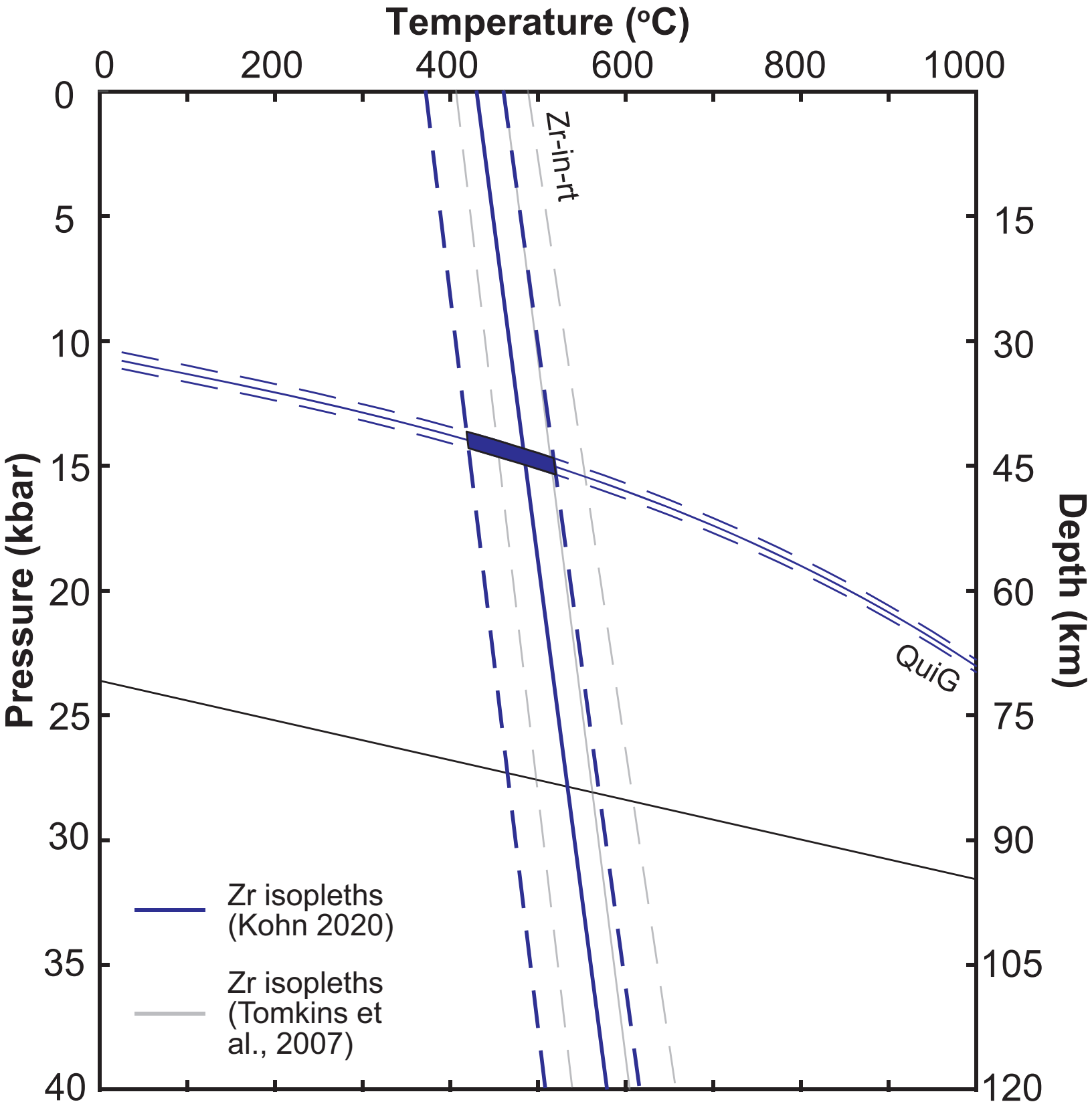
Temperature (°C)
0
200
400
600
800
1000
Pressure (kbar)
0
5
10
15
20
25
30
35
40
Depth (km)
15
30
45
60
75
90
105
120
Zr-in-rt
QuiG
Zr isopleths (Kohn 2020)
Zr isopleths (Tomkins et al., 2007)

Fig. S3

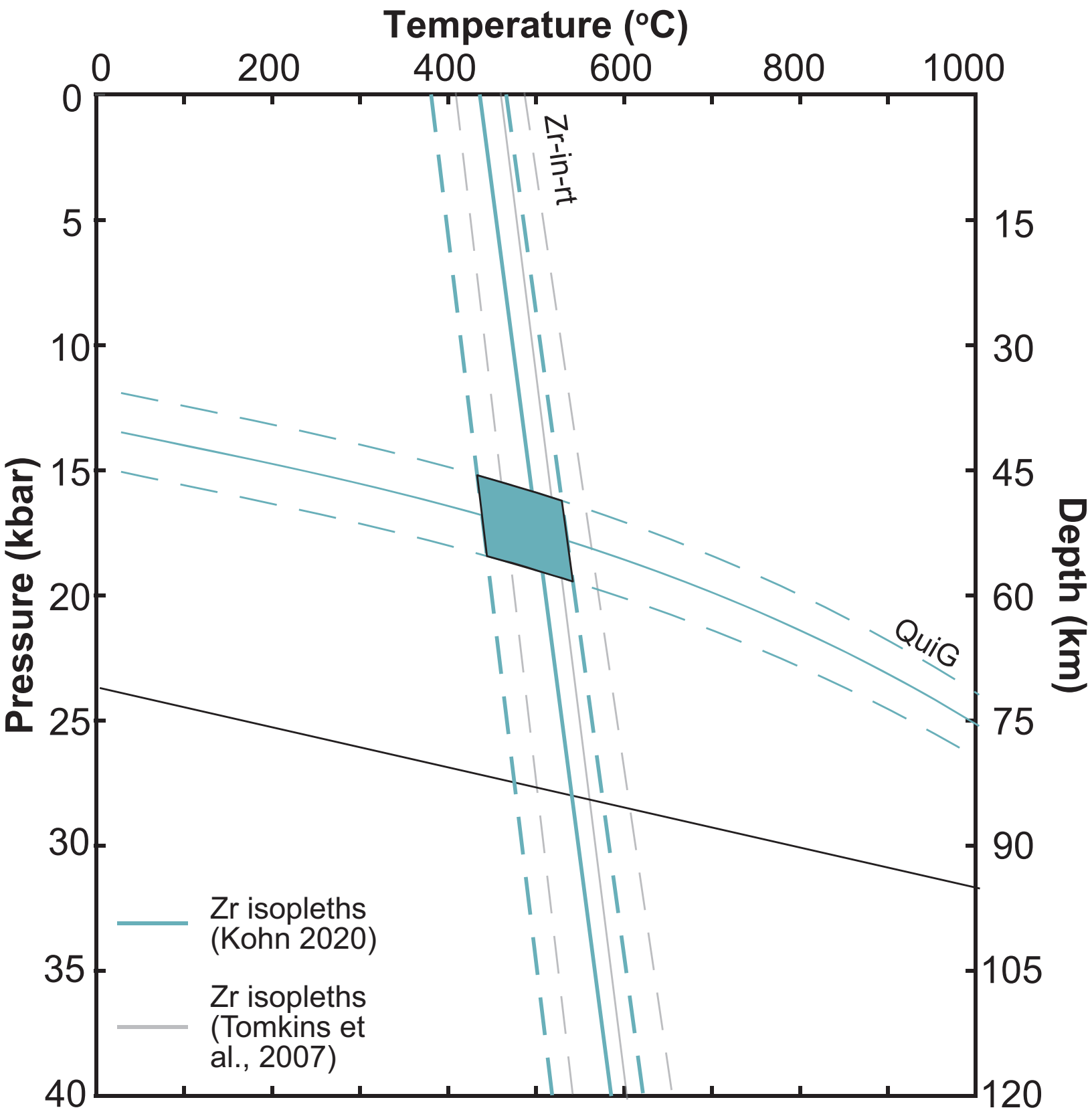
Temperature (°C)
0
200
400
600
800
1000
Pressure (kbar)
0
5
10
15
20
25
30
35
40
Depth (km)
15
30
45
60
75
90
105
120
Zr-in-rt
QuiG
Zr isopleths (Kohn 2020)
Zr isopleths (Tomkins et al., 2007)

Fig. S4

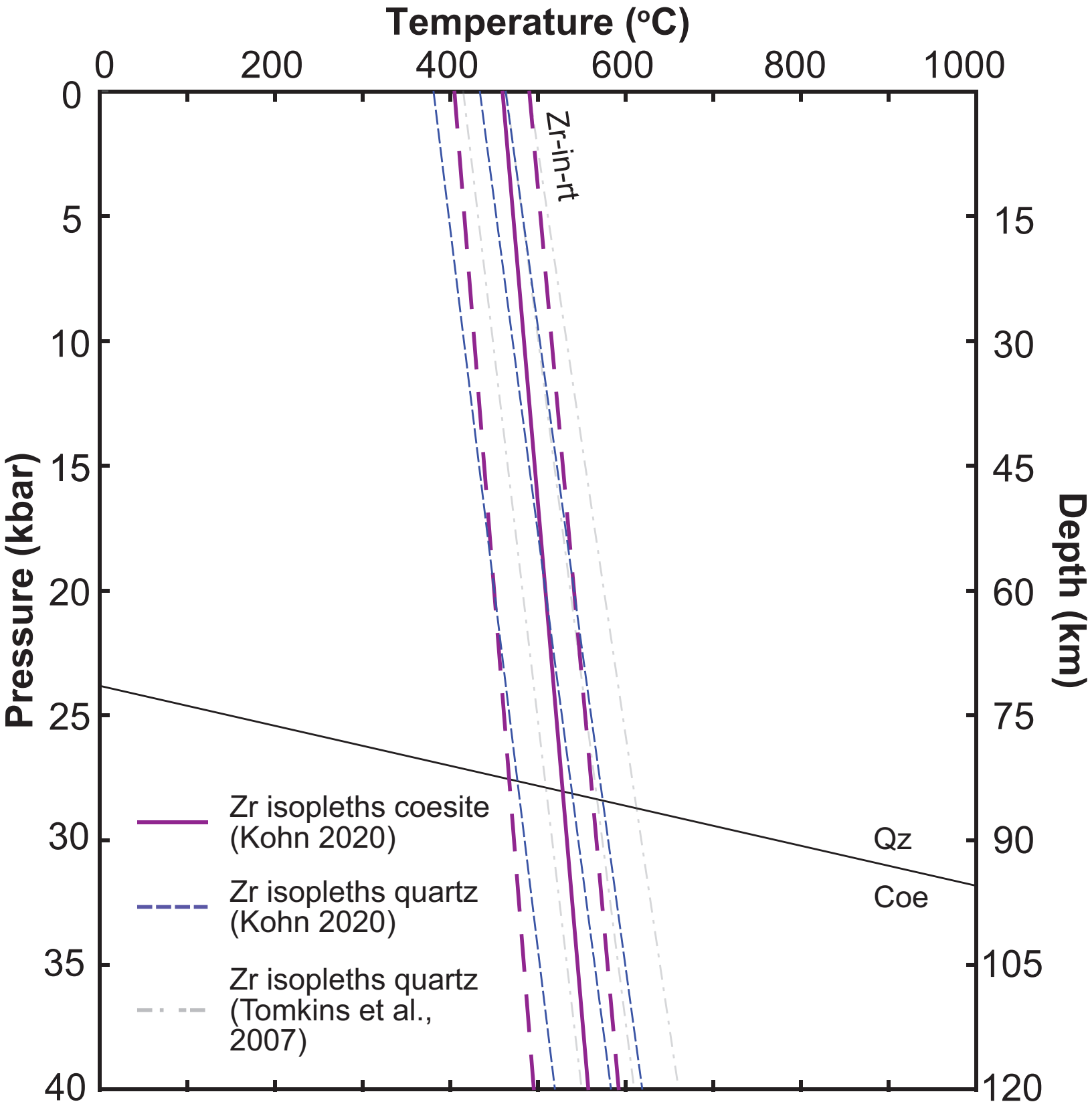
Temperature (°C)
0
200
400
600
800
1000
Pressure (kbar)
0
5
10
15
20
25
30
35
40
Depth (km)
15
30
45
60
75
90
105
120
Zr-in-rt
Zr isopleths coesite (Kohn 2020)
Zr isopleths quartz (Kohn 2020)
Zr isopleths quartz (Tomkins et al., 2007)
Qz
Coe

Fig. S5